Nanoscale

Accepted Manuscript

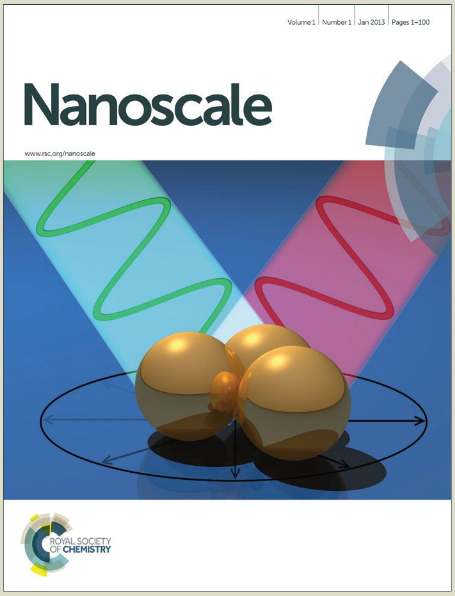

ROYAL SOCIETY OF CHEMISTRY

www.rsc.org/nanoscale

Controllable Assembly of Well-defined Monodisperse Au Nanoparticles on Hierarchical ZnO Microspheres for Enhanced Visible-Light-Driven Photocatalytic and Antibacterial Activity

Yuan Wang, [a] **Hua-Bin Fang,** [a] **Yan-Zhen Zheng,** *[a] **Rongqin Ye** [a], **Xia Tao,** *[a]
Jian-Feng Chen [b]

[a]State Key Laboratory of Organic-Inorganic Composites, Beijing University of Chemical Technology, Beijing 100029, China

[b]Research Center of the Ministry of Education for High Gravity Engineering & Technology, Beijing University of Chemical Technology, Beijing 100029, China

Abstract: A high-efficiency visible-light-driven photocatalyst composed of homogeneously distributed Au nanoparticles (AuNPs) well-defined on hierarchical ZnO microspheres (ZMS) via a controllable layer-by-layer self-assembly technique is demonstrated. The gradual growth of the characteristic absorption bands of Au loaded on ZnO in visible region with increasing number of assemblies indicates the enhancement of the light harvesting ability of the ZMS/Au composites as well as the reproducibility and controllability of the entire assembly process. Results on the photoelectrochemical performance characterized by EIS and transient photocurrent response spectra indicate that the ZMS/Au composites possess increased photoinduced charge separation and transfer efficiency compared to the pure ZMS film. As a result, the hybrid composites exhibited enhanced decomposition activity for methylene blue and salicylic acid as well as the antibacterial activity in killing S. aureus and E. coli under visible irradiation. Notably, well-distributed Au components even at a rather low Au/ZnO weight ratio of ~ 1.2% also exhibited extraordinary photocatalysis. Such a facile and controllable self-assembly approach may be viable for preparing high-performance visible-light-driven ZMS/Au photocatalyst in a simple and controllable way, and consequently, extendable to other plasmon-enhanced heterostructures made of nanostructured semiconductors and noble metals for great potential application in environmental protection.

Introduction

Solar photocatalysis for remediation of environmental pollutants and hydrogen production from water has attracted a tremendous amount of interest over the past decades as it offers direct use of sunlight for energy and environmental applications.[1-3] Among many photocatalysts developed to date, zinc oxide (ZnO) has been regarded as one of the most promising photocatalysts owing to its wide band gap (E_g = 3.37 eV), large exciton binding energy (60 meV), high carrier mobility (~205-1000 $cm^2\ V^{-1}\ s^{-1}$), non-toxicity, abundant availability, and easy surface tailor ability.[4, 5] However, its large band gap means that ZnO is only active in the ultraviolet (UV) region, which accounts for less than 5% of the total energy of the solar spectrum.[6] Besides, the rapid recombination of photogenerated electron-hole pairs (typically in ps-μs) in pristine ZnO due to the direct band gap in the photocatalytic process often leads to a decreased photocatalytic activity.[7] The combination of ZnO nanomaterials with noble metals to form metal/semiconductor hybrid nanostructures has recently been proposed as a way to increase photocatalytic efficiency.[8, 9] This is because noble metal nanoparticles may increase the photoenergy conversion efficiency of ZnO by (1) increasing the efficiency of charge carrier separation and achieving Fermi level equilibrium, and (2) extending light harvesting and facilitating creation of electron-hole pairs induced by the surface plasmon resonance (SPR) effect.[10-12] Noble metal nanoparticles (e.g. Au, Ag and Pt NPs) are usually chosen to form such hybrid structures to obtain enhanced photocatalytic activity, with Au-ZnO having been particularly well-studied owing to its high stability and strong visible-light absorption over a wide solar spectrum range.[13-19] For example, Gong and co-workers synthesized AuNPs sensitized ZnO nanopencil arrays via an aqueous chemical growth and subsequent photoreduction method for photoelectrochemical water splitting.[20] Li et al. prepared Au-ZnO hybrid NPs with a hexagonal pyramid-like structure and study the photocatalytic degradation of rhodamine B (RhB) under UV illumination.[21] Herring et al. described assembly of Au-ZnO nanopyramids using microwave irradiation and study the formation mechanism of the heterostructure.[22] In most cases, the preparation methods mainly focus on aqueous chemical growth and subsequent in situ formation of Au anchored to ZnO matrix. Such synthetic protocols will inevitably cause particle aggregation and thus lead to the reduction of photocatalytic activity. Very recently, Wu et al. reported a precisely controlled synthesis of a highly efficient photocatalyst composed of unaggregated AuNPs chemically bound to vertically aligned ZnO nanorod arrays via a bifunctional surface molecular linker.[23] Though the preformed heterostructures exhibited a higher photodegradation rate compared to ZnO due to the UV light-induced electron transfer from the conduction band of ZnO to lower Fermi level, the preparation procedures of unaggregated Au NPs-decorated ZnO are a little more complicated. Furthermore, the photocatalytic degradation of substrates was carried out in the UV light-induced reaction system. However, as a matter of fact, plasmon-excited hot electrons in Au NPs under visible-light irradiation can be transferred to the conduction band of an adjacent ZnO over the Schottky barrier, and then participate in subsequent reactions.[11] As such, study on visible light (a large fraction of solar spectrum, ~43%) as well as subsequent separation and reaction of photogenerated electron-hole pairs under visible-light irradiation is of particular importance for further improvement of the Au-ZnO plasmonic photocatalytic activity.

It has been demonstrated that electrostatic LBL self-assembly, as a versatile bottom-up nanofabrication technique, possesses prominent merits over conventional approaches on versatility of the use of various organic-inorganic materials and simplicity of solution-processed fabrication, and furnishes molecular-level control over the thickness, structure, and composition of the multilayered films with simple benchmark operations.[24] Meanwhile, it should be mentioned that surface-modified AuNPs or negatively-charged Au precursor provide new options for LBL assembly of various high-quality AuNPs based hybrid films.[25, 26] In this regard, we herein develop a LBL self-assembly approach to synthesize high-efficiency visible-light-driven photocatalysts composed of monodispersed AuNPs bonded to the surface of ZMS through electrostatically alternate adsorption of positively-charged poly (ethyleneimine) (PEI) and negatively-charged Au precursor ($AuCl_4^-$) and subsequent heating reduction, as shown in Fig. 1. It was found that the AuNPs were monodispersed and well-defined on the surface of ZMS, and hence allowing more activity sites. The gradual growth of the characteristic absorption bands of Au loaded on ZnO in visible region with increasing number of assemblies indicates the increase of the light harvesting ability of the hybrid composites as well as the reproducibility and controllability of the assembly process. Herein, ZMS/Au hybrid nanostructures having different weight ratios of Au to ZnO were synthesized. The photocatalytic activity of as-synthesized Au-ZMS was evaluated by the decomposition of organic pollutants i.e. methylene blue (MB) and salicylic acid (SA) as well as the activity in killing bacteria i.e. S. aureus and E. coli under visible irradiation. Compared to pure ZnO, ZMS/Au exhibited plasmonic activity because of the presence of SPR in the Au NPs. Notably, Au nanocomponents even at very low ZnO/Au weight ratio of 1.2% can greatly enhance the visible-light-driven photocatalytic and antibacterial activity of ZnO. This enhanced photocatalytic activity is also discussed in terms of enlarged light harvesting, effective charge separation/transfer/transport and assembled layer numbers.

Experimental section

2.1. Sample preparation

All chemicals used were analytical grade reagents without further purification. To synthesize ZnO/Au heterostructures, hierarchical ZMS was firstly synthesized *via* a facile and surfactant-free chemical solution route. The detailed synthesis procedure of ZMS was as follows: 10.0 mmol zinc nitrate hexahydrate ($Zn(NO_3)_2 \cdot 6H_2O$, Aldrich) were dissolved in 160 mL of deionized water. Then 30 mmol NaOH was added into the above solution to keep pH ~ 13 and then stirred continuously for 3 h at room temperature. The ZMS product was obtained via filtration, rinsing with ethanol, drying at 60 ˚C in air for 12 h and finally annealing at 450 ˚C in air for 2 h. For synthesizing ZMS film, a colloid solution containing ZMS, ethyl cellulose and terpineol with a weight ratio of 1:0.15:1.5 was prepared and subsequently coated on a fluorine-doped tin oxide (FTO) glass substrate *via* a typical doctor blading method. Afterwards, by means of using a LBL self-assembly process, ZMS/Au was prepared (Fig. 1). Typically, the ZMS films were immersed in 50 mL of H_2O containing 0.05g of poly ethyleneimine (PEI, $(CH_2CH_2NH)_n$) for 10 min. Excess PEI was removed by rinsing. The obtained PEI-anchored ZMS film was then immersed in 50 mL of $HAuCl_4$ aqueous solution (1mg/mL) for 10 min. After rinsing for several times and drying in air, the ZMS-PEI-$AuCl_4^-$ film was then calcined at 550 °C in air atmosphere to form ZMS/Au hybrid film, accompanied by the removal of the PEI.

2.2. Characterization

The crystalline structure of the as-synthesized ZMS and ZMS/Au films was identified by X-ray diffraction analysis (XRD) (X'Pert PRO MPD, Panalytical) using Cu Kα radiation. The surface morphology of the as-prepared films was determined from scanning electron microscope (SEM) images on a Hitachi S-4700 microscope and high-resolution transmission electron microscopy (HRTEM) images characterized on a JEOL JEM-3010 microscope. An energy-dispersive spectroscopy (EDS) measurement was performed with an X-ray energy dispersive spectrometer installed on a JEOL-6701F microscope. The absorption spectra were measured using UV-vis spectrophotometry (Lambda 950, Perkin Elmer). The chemical compositions of ZnO/Au hybrid film were determined by X-ray photoelectron spectroscopy (XPS) performed on a thermo ESCALAB250 XPS system using an Al Kα X-ray source. The overall composition and spatial distribution of the Au, Zn and O in a selected area was further investigated by scanning transmission electron microscopy elemental mapping with an X-ray energy dispersive spectrometer installed on a Hitachi S-4700 microscope. Steady state photoluminescence (PL) measurements were acquired using an Edinburgh Instruments FLS920 fluorescence spectrometer. Electrochemical and photoelectrochemical measurements were performed in a three-electrode quartz cell with a 0.5 M Na_2SO_4 electrolyte solution. A platinum wire was used as the counter electrode, a saturated calomel electrode (SCE) was used as the reference electrode, and the as-prepared photocatalyst film was used as the working electrode. Samples were irradiated in the visible range using a 500 W Xe lamp (Institute for Electric Light Sources, Beijing) with a 420 nm cut-off filter. Potentials were given with reference to the SCE. The on-off light photoresponse of the photocatalysts was measured at a 0.0 V bias. Electrochemical impedance spectra (EIS) were measured at 0.0 V. A sinusoidal AC perturbation of 5 mV was applied to the electrode over the frequency range of 0.05-10^5 Hz.

2.3. Photocatalytic activity test

The photocatalytic activities of ZMS and various ZMS/Au hybrid films were evaluated by measuring the degradation of methylene blue (MB) and salicylic acid (SA) in aqueous solutions under visible light irradiation ($\lambda > 420$ nm) using a 500 W Xe lamp with a 420 nm cutoff filter. 6.0 cm^2 of ZMS or various ZMS/Au hybrid films was dispersed in a 40 mL aqueous solution containing 3.0 × 10^{-2} mM MB or 1.5 × 10^{-2} mM SA. First, the solution was continuously stirred in the dark for about 1 h to establish an adsorption-desorption equilibrium between the photocatalyst and substrates. During degradation testing, the MB or SA solution with the photocatalyst film was continuously stirred using a dynamoelectric stirrer and the concentration of the dye was monitored by colorimetry with a UV-vis spectrophotometer.

2.4. Antibacterial activity test

The bacterial cultures of Escherichia coli (ATCC 25922) and Staphylococcus aureus subsp. aureus (ATCC 29213) were chosen as gram negative and positive model organisms, respectively, for antibacterial activity experiments. Both bacteria were grown overnight on BHIA (Brain Heart Infusion Agar, BD-Difco) plates in an incubator at 37°C. Bacterial growth was harvested using a sterilized swab and resuspended in the 1 × PBS buffer to achieve a viable cell concentration of about 1.5 to 2.0 × 10^7 cells/mL. This bacteria suspension was used as a stock suspension for antibacterial activity assay of prepared photocatalytic samples in a reaction chamber. 500 µl of the bacterial stock suspension was dropped on each ZMS or various ZMS/Au heterostructures, and then the films containing bacteria and phtocatalysts were irradiated under visible light irradiation ($\lambda > 420$ nm) using a 500 W Xe lamp with a 420 nm cutoff filter for 20 min. The photocatalysts and survival bacteria on each film were then serially diluted and 500 µl from each dilution was spread onto BHIA agar plates. The plates were incubated at 37°C overnight, then the resulting bacterial growth was enumerated in colony forming units. The bacteria survival rate was calculated as follows:

Survival rate (%) = $100 \times N/N_0$,

where N is the number of colony forming units measured after plating cells irradiated in the presence of phtocatalysts, and N_0 is the number of colony forming units measured after plating cells exposed to neither phtocatalysts nor visible light irradiation. All assays were conducted in triplicate and repeated at least twice to confirm reproducibility.

Results and discussion

Fig. 2 shows the SEM and HRTEM images of the ZMS and the ZMS/Au heterostructures with AuNPs fabricated via the LBL self-assembly method. The pure ZMS displays a hierarchical sphere-like structure with diameters varying from 2~4 μm (Fig. 2a). A magnified SEM image of an individual aggregate (in the insert of Fig. 2a and Fig. 2b) shows that the ZMS secondary microsphere consists of packed nanosheets with ~20 nm thickness. Such hierarchical architecture indeed may provide more reaction space allowing substrate molecules to readily diffuse into or out of the nanosheet aggregates based ZMS. The HRTEM image (Fig. 2c) reveals that the each ZMS sheet is single-crystalline in wurtzite crystal structure.[27] After the alternative LBL self-assembling of PEI and $HAuCl_4$ and thermal treatment, the structural features of the ZMS/AuNPs system remain constant except for the bright spots of well-dispersed on the ZMS surface, as shown in the SEM images (Fig. 2d-e). HRTEM image from a part of the ZMS/AuNPS system shows well-resolved Au (111) (0.24 nm) and ZnO (002) (0.26 nm) crystalline lattices indicating the highly crystalline nature of ZMS and Au NPs.[7] A close contact between them is beneficial to electron transfer from the excited AuNPs to the conduction band of ZnO. The film thickness of as-fabricated ZMS/$AuNP_S$ was determined as 25 μm (Supporting Information Fig. S1). The corresponding cross sectional SEM images (Fig. 2g-i) clearly show that AuNPs are well-dispersed on the whole hybrid film.

The overall composition and spatial distribution of Au in the heterostructure film was further investigated by SEM elemental mapping scanning from the selective area of Fig. 3a. The Zn, O and Au peaks can be easily observed (Fig. 3b). Notably, no peaks observed for C, N, and H demonstrated that the PEI no longer exist in the ZMS/Au hybrid film. Fig. 3c-e shows the elemental mapping for Zn, O, Au atoms. The homogeneous spatial distribution of Au within the ZnO matrix is clearly discernible, which is attributed to the controllable deposition of alien species via the LBL self-assembly process. The mechanism for the formation of ZMS/AuNPs heterostructures via PEI polyelectrolyte-involving LBL technique can be summarized as follows: In the assembly process, the positively charged PEI molecules were first introduced onto the surface of hierarchical ZnO through a strong electrostatic affinity and interaction between the hydroxyl and the amine groups.[25, 28] Then Au precursor ($AuCl_4^-$) were electrostatically adsorbed on the hierarchical ZnO-PEI. The strong interaction between $AuCl_4^-$ and the amine groups within PEI is advantageous to a homogeneous deposition of Au precursor with a considerable quantity on each ZnO nanosheet.[29] The obtained hybrid composite was then calcined at 550 °C to convert adsorbed $AuCl_4^-$ into AuNPs and at one time remove the PEI. Note that the morphology of ZMS heterostructures remained unchanged after the LBL self-assembly process. For comparison, ZMS/AuNPs heterostructures via a PEI-free LBL self-assembly method as a control was also synthesized following the same preparation procedures as above, except without the introduction of PEI. From the corresponding SEM image (Supporting Information Fig. S3), one can see that only a few AuNPs disperse on the surface of ZMS and this identifies the key role of amine groups-rich PEI in assembling efficient and uniformly-dispersed AuNPs on the surface of ZMS.

Fig. 4a-c schematically displays the deposition of AuNPs onto the surface of hierarchical ZMS by the LBL self-assembly method upon various assembly numbers i.e. one-round, two-round, and three-round, which are donated as ZMS/AuNPs-1, ZMS/AuNPs-2, and ZMS/AuNPs-3 films, respectively. The corresponding SEM and TEM images (Fig. 4d-i) clearly show that the morphology of ZMS-AuNPs heterostructures remained unchanged and AuNPs with sizes from 10 nm to 25 nm well-dispersed on the ZMS even in the ZMS/AuNPs-3 with 4.5 wt % AuNPs. Fig. S2a-c presents intimate contact between Au and ZMS in all three various ZMS/Au hybrid structures. As exhibited in Fig. 4j-l, Au elemental mapping of the ZMS/Au hybrid films demonstrate that 1.2, 2.3, and 4.5 wt% of Au are uniformly distributed in the ZMS/AuNPs-1, ZMS/AuNPs-2, and ZMS/AuNPs-3 films, respectively. Apparently, the Au content in the ZMS/AuNPs heterostructures increases proportionally to an increase of the LBL assembly numbers from 1 to 3 round, which allows more activity sites. All above results demonstrate that the fabricated ZMS-AuNPs possess several desirable features for highly efficient photocatalyst applicable in environmental purification i.e. the well dispersion of AuNPs on the ZMS surface without aggregation, the good morphology control, and the accurate control of the Au loading, and all of three are in a scalable and controllable manner via facile LBL self-assembly technique.[30]

The representative XRD patterns, as shown in Fig. 5, examined the crystal phase and crystalline of ZMS and ZMS/AuNPs samples. All the clear diffraction peaks of both ZMS and ZMS/AuNPs samples may be indexed to the standard pattern of hexagonal ZnO phase (JCPDS No. 36–1451), in good agreement with the SEM observations in Fig. 2. As for ZMS/AuNPs, one can observe the typically peaks at 38.37°, 77.21°, 44.62° ascribed to Au (111), Au (311) and Au (200), respectively. The presence of major Au (111), Au (311) and minor Au (200) planes in the diffraction patterns further demonstrates the formation of crystalline AuNPs on the ZMS.[31] The surface chemical states of Au, O and Zn in ZMS/AuNPs were investigated via high resolution XPS measurements, and the results are provided in Fig 6a-c. The binding energy peaks of Zn 2p of the ZMS/AuNPs observed at around 1021.6 and 1044.5 eV may be attributed to those of Zn $2p_{3/2}$ and Zn $2p_{1/2}$, respectively (Fig. 6a). The XPS core level spectra of O_2^- in the ZMS/AuNPs sample are displayed in Fig. 6b. It can be seen that an intense peak ascribed to O 1s of ZMS/AuNPs centers at 530.3 eV.[32, 33] The peak located at a binding energy of 83.2 eV is assigned to metallic Au $4f_{7/2}$, indicating that the Au species exist as metallic Au^0 in ZMS/AuNPs.[25] In comparison with bulk Au ($4f_{7/2}$ at 84.0 eV), a negative shift of 0.8 eV could be found for the Au $4f_{7/2}$ peak in ZMS/AuNPs, probably resulting from metal-support interactions between the AuNPs and the ZMS.[23, 34] Such similar negative shift of binding energy has also been observed in other AuNPs decorated TiO_2 or ZnO systems.[23]

The optical properties of ZMS/AuNPs along with that of the reference ZMS sample were investigated using steady-state diffuse reflectance UV-vis spectroscopy and UV–vis absorption spectra. As shown in Fig. 7, the reflection spectra for all four samples attenuate sharply at wavelengths shorter than 380 nm, originated from strong intrinsic light absorption in the ZnO semiconductor. The gold decoration does not trigger remarkable difference in ZnO band gap. In case of the ZMS/AuNPs heterostructures, another decrease in diffuse reflectance and increase in absorption spectra located at around 548 nm can be distinctly observed, which matches well with the surface plasmon resonance (SPR) absorption of AuNPs.[23, 35] Note that the characteristic peak of AuNPs assembled on the ZMS is distinctly broadened and red-shifted by about 28 nm relative to the conventional AuNPs with a similar size distribution.[36] The observed shift can be attributed to the strong interaction between AuNPs and ZMS, which may alter the Au

SPR feature due to the change in the dielectric property of the surrounding microenvironment.[37] Furthermore, the SPR absorption of the ZMS/AuNPs heterostructures increases steadily with the increase of Au loading content, and hence facilitating the enhancement in the photocatalytic activity of ZMS/AuNPs.

Fig. 8 displays the PL spectra of the pristine ZMS and various ZMS/AuNPs films with an excitation wavelength of 340 nm. Pure ZMS as well as ZMS/AuNPs-1 composites showed a strong emission peak centered at ~393 and three weak emission peaks in the visible range. The sharp and intense ultra violet emission peak at 393 nm is attributed to the band gap excitation. The weak emission peaks centered in the visible range is ascribed to the trap-state emission of ZnO, which originated from the intrinsic defects such as oxygen vacancies in ZnO lattice.[38] The intensity of all emission peaks from ZMS/AuNPs-1 significantly diminishes as compared to bare ZMS, which implies a prohibited recombination of photoinduced charge carriers as well as reduced amount of intrinsic defects of ZnO induced by the AuNPs introduction.[39] Notably, no PL peaks were observed for ZMS/AuNPs-2 or ZMS/AuNPs-3. It has been demonstrated that the strong interaction between exciton and plasmon states in a metal−semiconductor hybrid nanostructure can result in such quenching in PL.[40] This significant quenching of the characteristic PL peaks of Au loaded on ZnO with increasing number of assemblies further indicates efficiently prohibited recombination of photoinduced charge carriers and removal of intrinsic defects, which may assist in improving the photoconversion performance of ZnO.[41]

The photocatalytic activity of ZMS and ZMS/AuNPs hybrid nanostructures was evaluated by degradation of two representative probes i. e. the organic dye methylene blue (MB) and the colorless pollutant salicylic acid (SA) under visible light irradiation ($420 < \lambda < 800$). Note that SA was chosen for the purpose of verifying the photoactivity was due to the SPR excitation of AuNPs rather than the sensitization of dye molecules. Temporal changes in the concentrations of MB and SA were monitored by examining the variations in the maximal absorption peak at 664 nm and 298 nm, respectively. Fig. S4 in the Supporting Information shows the dependence of the light absorbance on the irradiation time for the ZMS-AuNPs. The absorbance values of either MB or SA in the whole spectrum range from 200 to 800 nm are gradually reduced with increasing irradiation time, indicating the effectiveness and completeness of the photodegradation of pollutants.[42, 43] Comparative photodegradation rates of MB and SA over ZMS and ZMS/AuNPs hybrid films with different Au loading amounts are also provided in the Fig. 9. The degradation curve for all the samples is estimated as C/C_0 versus time, where C_0 is the initial concentration of dye and C is the concentration after photo irradiation. It can be seen that no obvious degradation can be observed without catalyst. The degradation of MB and SA are both significantly enhanced after Au modification even at a very low Au/ZnO molar ratio of 1.2 wt%. Moreover, ZMS/AuNPs with a higher Au loading amount exhibits exceedingly excellent photocatalytic performance. The final degradation efficiency of the ZMS/AuNPs-3 sample reaches up to ~ 98% after 2 h of irradiation for MB and ~ 78% after 6 h for SA, which are superior to that of the ZMS (only ~ 60% for MB and ~ 26% for SA). Therefore, it can be concluded that the visible-light-driven degradation of organic pollutants was mainly induced by the SPR excitation of AuNPs assembled on the ZMS.

Apart from photocatalytic degradation of organic pollutants, the effect of Au deposition on the photobiological activity of the ZMS film was also examined. Herein, two representative bacteria able to cause an infectious disease of the mammary gland, gram positive S. aureus and gram negative E. Coli, were selected to investigate the antibacterial ability of the ZMS/AuNPs hybrid films.[44] Fig. 10 exhibits the ability of ZMS and ZMS/AuNPs hybrid nanostructure films in killing S. aureus (a) and E. coli (b) before and after irradiation with visible light illumination for 20 min. Both the S. aureus and E. coli grew well in the absence of catalyst film and irradiation (Fig. 10, Blank). Irradiation with visible light caused a decrease in bacterial survival (Fig. 10, No film), exposure to ZMS film alone, without irradiation, resulted in slight decreased bacterial survival compared to blank. When exposing on ZMS film, the survival of both S. aureus and E. coli decreased further after irradiation for 20 min. Note that the pristine ZMS presents relatively lower antibacterial activity than those results reported elsewhere, probably due to films used herein instead of conventional particles and/or visible light source used herein as an alternative to simulated sunlight.[10, 15] A similar negligible antibacterial activity of ZnO nanorod and ZnO nanospherical under visible light irradiation has been reported by Rao and co-workers.[45] When exposing to ZMS/AuNPs films alone as compared to pure ZMS, it can be clearly seen that the survival of both S. aureus and E. coli was further decreased. Notably, the survival of S. aureus and E. coli reached ~3% and ~1% after irradiation for 20 min, a rate much less than of ZMS film (~95% for S. aureus and ~96% for E. coli). In addition, the observed antibacterial activity also increased with increasing AuNPs on ZMS film, resulting in almost complete bacteria killing in the presence of ZMS/AuNPs-2 and ZMS/AuNPs-3 under visible illumination of 20 min.

The hybrid ZMS/Au films show enhanced photodegradation activity and antibacterial activity, which most likely, to some extent, comes as a result of extended light harvesting induced by the SPR effect as proved via the UV-vis reflection spectra. In order to further prove the SPR effect of the Au nanoparticles, the photocurrent density-voltage curves of ZMS and ZMS/AuNPs-3 (denoted as ZMS/Au) films were tested under the illumination of visible light ($\lambda > 420$ nm). It could be seen in Fig. 11 that the ZMS generates no obvious photocurrent both in dark and under illumination, which indicates that ZnO has no response to visible light. However, an enhancement in photocurrent is observed in ZMS/Au film, demonstrating the strengthened visible light response after the AuNPs introduction. As a result, such enhanced photocurrent response for the ZMS/Au likely explains the increase in visible light photocatalytic activity during MB and SA degradation as evidenced in Fig. 9a and b.[20]

The photoelectrochemical performance i.e. the efficiency of photogenerated charge interface separation, detected via such as electrochemical impedance spectroscopy (EIS) as well as transient photocurrent responses spectra, can also be employed to explain the enhancement of photocatalytic performance. The EIS Nyquist plots of ZMS and ZMS/Au samples both with and without visible light irradiation were carried out to further investigate the interface charge separation efficiency (Fig. 12a). The semicircle at high frequency is characteristic of the charge transfer process and the smaller arc radius on the EIS Nyquist plot indicates an effective separation of photo-generated electron-hole pairs and a fast interfacial charge transfer process.[46] It could be seen that both ZMS and ZMS/Au exhibit one arc/semicircle, suggesting that only the surface charge transfer step is involved in the photocatalytic reaction.[20] Notably, the arc for ZMS/Au film is much smaller than that of ZMS both in dark and under illumination, suggesting that the AuNPs significantly enhances the interfacial charge mobility by reducing the recombination of charge carrier occurred on the ZMS/Au interface. The ZMS films present almost the same charge transfer resistance in dark and under radiation, which is also due to the disable visible response of pure ZnO. In addition, the transient photocurrent responses of the photocatalyst may directly correlate with the recombination efficiency of the photogenerated carriers. Fig. 12b presents the results of the transient photocurrent response obtained from the ZMS and ZMS/Au films under the visible light ($\lambda > 420$ nm). The photocurrent intensity remains constant when the light is on and rapidly decreases to zero once the light is turned off. It is clear that the photocurrent of the ZMS/Au is greatly improved and is approximately 1.5 time that of the pure ZMS over several on-off cycles with good reproducibility. The enhanced photocurrent activity of the ZMS/Au film indicates more efficient separation of photoinduced charge carrier than in the pure ZMS film. This result is consistent with the EIS and PL results, and demonstrates that the high photocatalytic performance of ZMS/AuNPs also originates from its efficient separation of photoinduced charge carriers.[23, 47, 48]

Conclusion

In summary, we have demonstrated the construction of well-defined monodisperse AuNPs on hierarchical ZnO microspheres film via a facile LBL self-assembly process. The AuNPs loaded on ZnO show a gradual growth of the characteristic absorption bands in visible-light region with increasing number of assemblies indicates the enhancement of the light harvesting ability of the ZMS/Au composites as well as the reproducibility and controllability of the entire assembly process. The photoelectrochemical performance i.e. the efficiency of photogenerated charge interface separation, detected via such as EIS and transient photocurrent responses spectra demonstrates that the ZMS/Au composites possess higher charge separation as well as faster photoinduced charge carriers transfer efficiency. Owing to these synergic advantages, the designed ZMS/AuNPs films even at a rather low Au/ZnO weight exhibit significantly enhanced photocatalytic activities for organic dye degradation and antibacterial under visible irradiation compared to bare ZMS films. The facile and controllable assembly approach reported here is anticipated to be extendable for the fabrication of many other types of advanced semiconductor/noble metals hybrid films for a wide range of photocatalytic applications.

Acknowledgements

The work was supported by the National Natural Science Foundation of China (Nos. 21176019, 21377011, 21476019) and Beijing Higher Education Young Elite Teacher Project (YETP0487).

References

1 H. Kisch, *Angew. Chem. Int. Ed.*, 2013, **52**, 812-847.

2 Y. Zhao, W. Ma, Y. Li, H. Ji, C. Chen, H. Zhu and J. Zhao, *Angew Chem Int. Ed.*, 2012, **51**, 3188-3192.

3 F. Wang, C. Li, Y. Li and J. C. Yu, *Appl. Catal. B*, 2012, **119-120**, 267-272.

4 Q. Zhang, C. S. Dandeneau, X. Zhou and G. Cao, *Adv. Mater.*, 2009, **21**, 4087-4108.

5 X.-H. Lu, Y.-Z. Zheng, S.-Q. Bi, Y. Wang, X. Tao, L. Dai and J.-F. Chen, *Adv. Energy Mater.*, 2014, **4**, 1301802.

6 Y.-Z. Zheng, X. Tao, Q. Hou, D.-T. Wang, W.-L. Zhou and J.-F. Chen, *Chem. Mater.*, 2011, **23**, 3-5.

7 J. S. DuChene, B. C. Sweeny, A. C. Johnston-Peck, D. Su, E. A. Stach and W. D. Wei, *Angew. Chem. Int. Ed.*, 2014, **53**, 7887-7891.

8 R. Jiang, B. Li, C. Fang and J. Wang, *Adv. Mater.*, 2014, **26**, 5274-5309.

9 J. Gong, T. Zhou, D. Song and L. Zhang, *Sens. Actuators B*, 2010, **150**, 491-497.

10 W. He, H.-K. Kim, W. G. Wamer, D. Melka, J. H. Callahan and J.-J. Yin, *J. Am. Chem. Soc.*, 2014, **136**, 750-757.

11 M. Misra, P. Kapur and M. L. Singla, *Appl. Catal. B*, 2014, **150-151**, 605-611.

12 S. Sarina, E. R. Waclawik and H. Zhu, *Green Chem.*, 2013, **15**, 1814.

13 Z. Bian, T. Tachikawa, P. Zhang, M. Fujitsuka and T. Majima, *J. Am. Chem. Soc.*, 2014, **136**, 458-465.

14 J. Fei and J. Li, *Adv Mater.*, 2015, **27**, 314-319.

15 W. He, H. Wu, W. G. Wamer, H.-K. Kim, J. Zheng, H. Jia, Z. Zheng and J.-J. Yin, *ACS Appl. Mater. Interfaces*, 2014, **6**, 15527-15535.

16 X. Hou, *Materials Letters*, 2014, **137**, 319-322.

17 M. E. Aguirre, G. Custo, M. S. Goes, P. R. Bueno, G. Zampieri and M. A. Grela, *J.*

Phys. Chem. C, 2014, **118**, 2018-2027.

18 W. L. Ong, S. Natarajan, B. Kloostra and G. W. Ho, *Nanoscale*, 2013, **5**, 5568-5575.

19 J. Zhang, Y. Wu, M. Xing, S. A. K. Leghari and S. Sajjad, *Energy Environ. Sci.*, 2010, **3**, 715-726.

20 T. Wang, R. Lv, P. Zhang, C. Li and J. Gong, *Nanoscale*, 2015, **7**, 77-81.

21 P. Li, Z. Wei, T. Wu, Q. Peng and Y. Li, *J. Am. Chem. Soc.*, 2011, **133**, 5660-5663.

22 N. P. Herring, K. AbouZeid, M. B. Mohamed, J. Pinsk and M. S. El-Shall, *Langmuir*, 2011, **27**, 15146-15154.

23 T. H. Yang, L. D. Huang, Y. W. Harn, C. C. Lin, J. K. Chang, C. I. Wu and J. M. Wu, *Small*, 2013, **9**, 3169-3182.

24 X. Tao and J. Su, *Curr. Nanosci.*, 2008, **4**, 308-313.

25 C. T. Dinh, H. Yen, F. Kleitz and T. O. Do, *Angew. Chem. Int. Ed.*, 2014, **53**, 6618-6623.

26 O. L. Stroyuk, V. M. Dzhagan, A. V. Kozytskiy, A. Y. Breslavskiy, S. Y. Kuchmiy, A. Villabona and D. R. T. Zahn, *Mat. Sci. Semicon. Proc.*, 2015, **37**, 3-8.

27 Y.-Z. Zheng, X. Tao, L.-X. Wang, H. Xu, Q. Hou, W.-L. Zhou and J.-F. Chen, *Chem. Mater.*, 2010, **22**, 928-934.

28 A. M. Diez-Pascual and A. L. Diez-Vicente, *ACS Appl. Mater. Interfaces*, 2014, **6**, 10132-10145.

29 J. D. Henao, Y.W. Suh, J. K. Lee, M. C. Kung and H. H. Kung, *J. Am. Chem. Soc.*, 2008, **130**, 16142-16143.

30 F. X. Xiao, J. Miao and B. Liu, *J. Am. Chem. Soc.*, 2014, **136**, 1559-1569.

31 X. Li, J. Liu, H. Guo, X. Zhou, C. Wang, P. Sun, X. Hu and G. Lu, *RSC Adv.*, 2015, **5**, 545-551.

32 C. J. Raj, K. Prabakar, S. N. Karthick, K. V. Hemalatha, M.-K. Son and H.-J. Kim, *J. Phys. Chem. C*, 2013, **117**, 2600-2607.

33 Y. Wang, Y. Z. Zheng, S. Lu, X. Tao, Y. Che and J. F. Chen, *ACS Appl. Mater. Interfaces*, 2015, **7**, 6093-6101.

34 B. Donkova, P. Vasileva, D. Nihtianova, N. Velichkova, P. Stefanov and D. Mehandjiev, *J. Mater Sci*, 2011, **46**, 7134-7143.

35 A. Naldoni, M. D'Arienzo, M. Altomare, M. Marelli, R. Scotti, F. Morazzoni, E.

Selli and V. Dal Santo, *Appl. Catal. B*, 2013, **130-131**, 239-248.

36 S. Link and M. A. El-Sayed, *J. Phys. Chem. B*, 1999, **103**, 4212-4217.

37 G. Manna, R. Bose and N. Pradhan, *Angew. Chem. Int. Ed.*, 2014, **53**, 1-5.

38 S. Bai, Y. Jin, X. Liang, Z. Ye, Z. Wu, B. Sun, Z. Ma, Z. Tang, J. Wang, U. Würfel, F. Gao and F. Zhang, *Adv. Energy Mater.*, 2015, **5**, 1401606.

39 X. Liu, Z. Li, W. Zhao, C. Zhao, J. Yang and Y. Wang, *J. Colloid Interface Sci.*, 2014, **432**, 170-175.

40 L. Ruiz Peralta Mde, U. Pal and R. S. Zeferino, *ACS Appl. Mater. Interfaces*, 2012, **4**, 4807-4816.

41 Y.-H. Lu, W.-H. Lin, C.-Y. Yang, Y.-H. Chiu, Y.-C. Pu, M.-H. Lee, Y.-C. Tseng and Y.-J. Hsu, *Nanoscale*, 2014, **6**, 8796-8803.

42 W. Ma, R. Ma, J. Liang, C. Wang, X. Liu, K. Zhou and T. Sasaki, *Nanoscale*, 2014, **6**, 13870-13875.

43 L. Ding, R. Wei, H. Chen, J. Hu and J. Li, *Appl. Catal. B*, 2015, **172**, 91-99.

44 W. Jin, E. M Ibeagha-Awemu, G. Liang, F. Beaudoin, X. Zhao and L. L. Guan, *BMC Genomics*, 2014, **15**, 181.

45 R. Kumar, S. Anandan, K. Hembram and T. Narasinga Rao, *ACS Appl. Mater. Interfaces*, 2014, **6**, 13138-13148.

46 F. Xiao, F. Wang, X. Fu and Y. Zheng, *J. Mater. Chem.*, 2012, **22**, 2868.

47 S. Liu, M.-Q. Yang, Z.-R. Tang and Y.-J. Xu, *Nanoscale*, 2014, **6**, 7193-7198.

48 Y. He, Y. Wang, L. Zhang, B. Teng and M. Fan, *Appl. Catal. B*, 2015, **168**, 1-8.

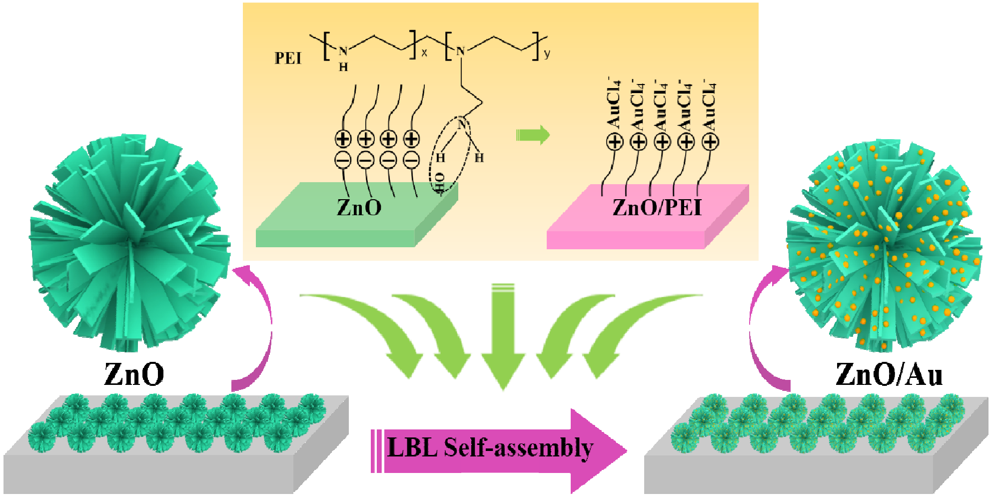

Fig.1. Schematic diagram of the formation for the ZMS/AuNPs heterostructures prepared on glass substrate.

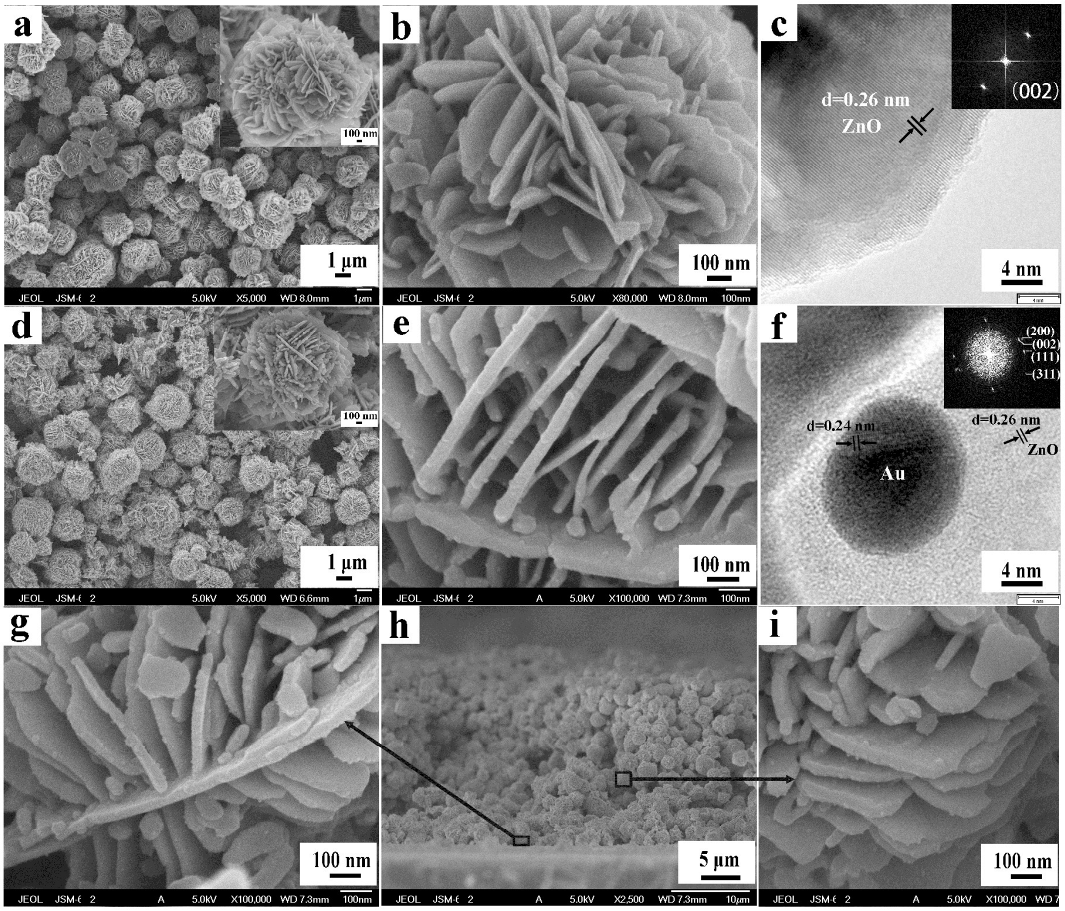

Fig. 2. (a) SEM images (inset is SEM of single ZMS), (b) high magnification top view and (c) HRTEM image (inset is SAED pattern) of ZMS; (d) SEM images (inset is SEM of single ZMS/Au), (b) high magnification top view and (c) HRTEM image (inset is SAED pattern) of ZMS/AuNPs-1. (h) Cross sectional SEM image of as-prepared ZMS/AuNPs-1 film, (g & i) High magnification cross sectional SEM images of selected area.

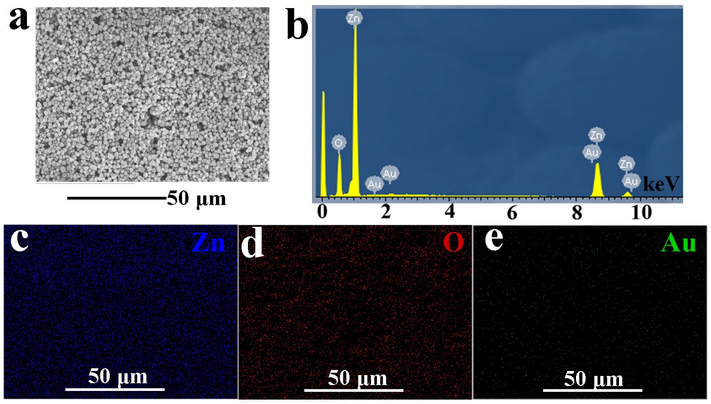

Fig. 3. (a) SEM image of selected area; (b) EDS; and EDS mapping profiles for the ZMS/AuNPs-1 with (c) Zn; (d) O; and (e) Au.

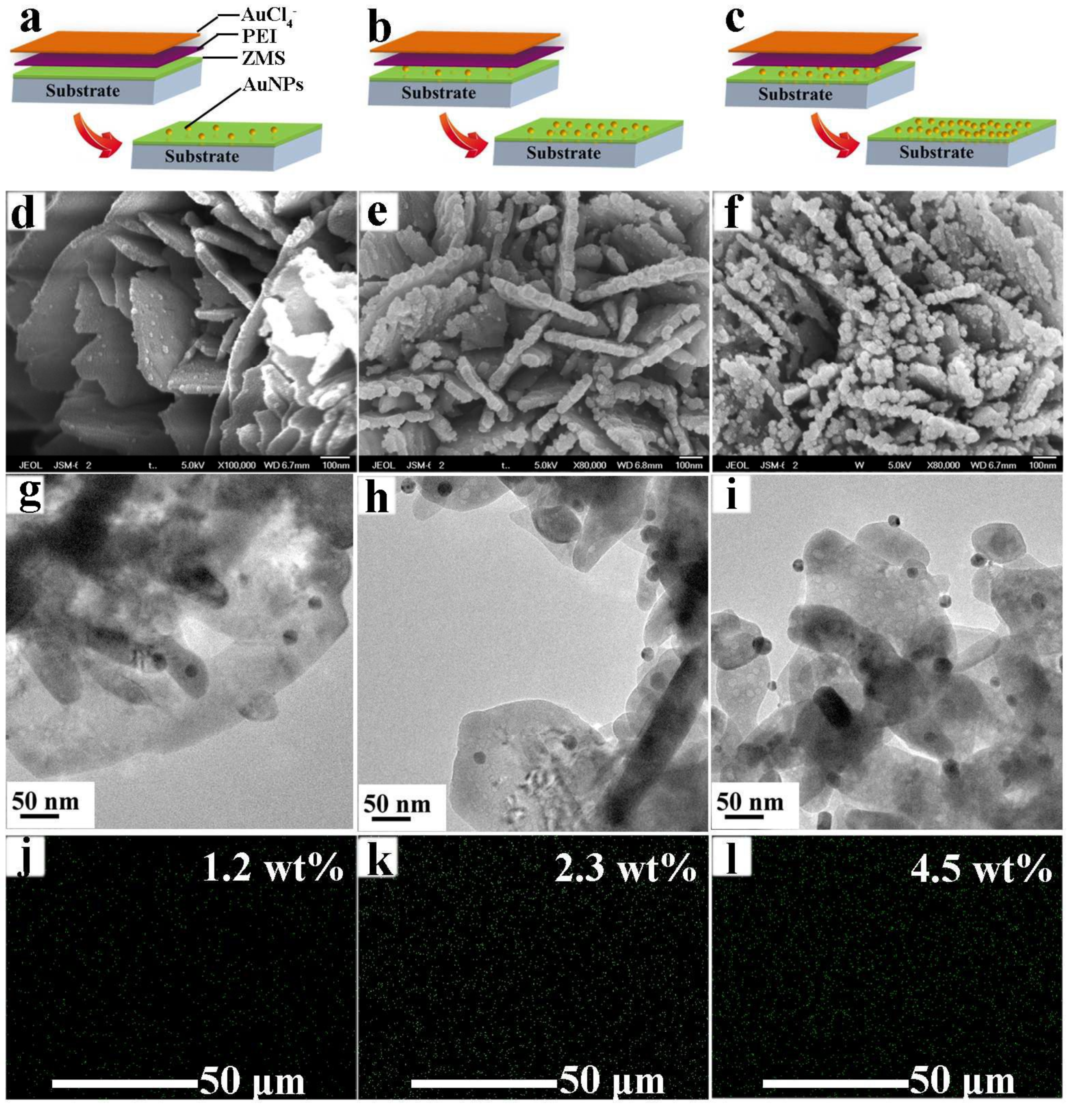

Fig. 4. (a-c) Schematic diagrams, (d-f) SEM images (g-i) TEM images and (j-l) EDS mapping profiles of Au element for the ZMS/AuNPs-1; ZMS/AuNPs-2; ZMS/AuNPs-3, respectively.

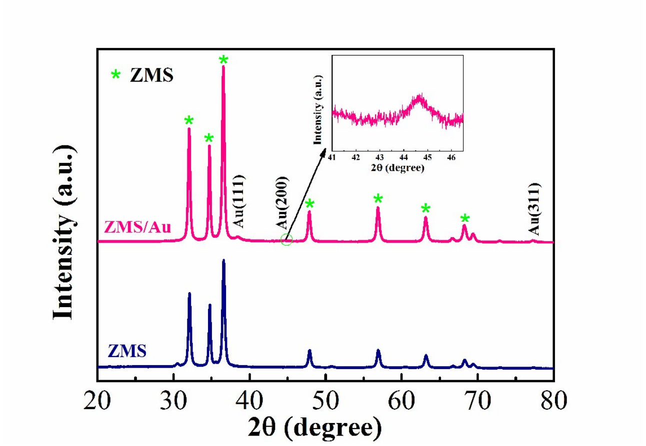

Fig. 5. XRD patterns of the ZMS and ZMS/AuNPs-3.

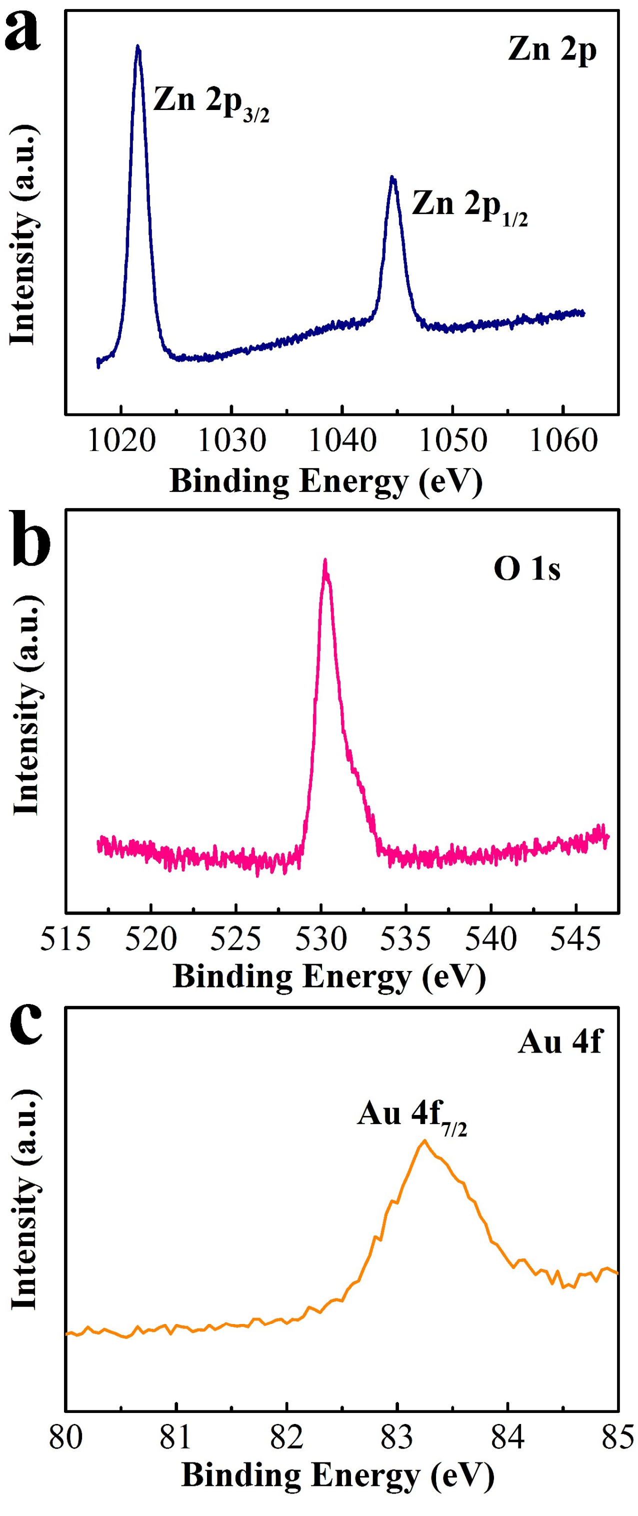

Fig. 6. XPS spectra: (a) Zn 2p; (b) O 1s; (c) Au 4f regions of the ZMS/AuNPs-3 sample.

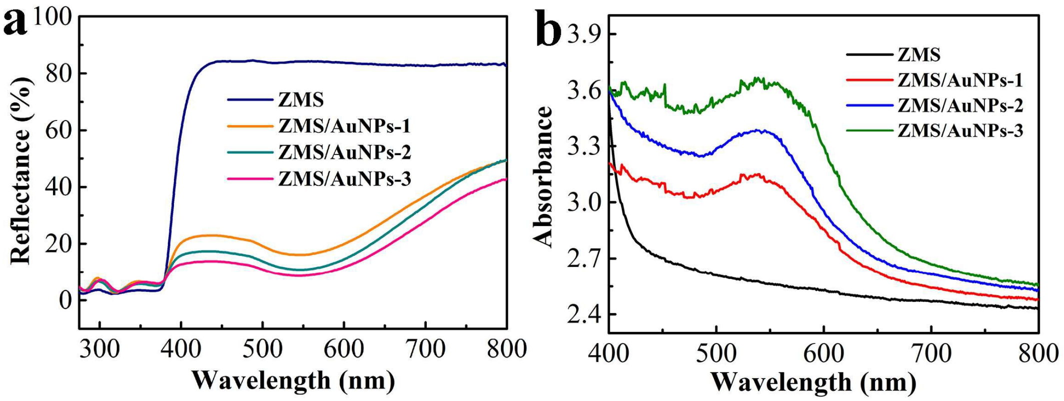

Fig. 7. UV/Vis diffuse reflectance spectra (a) and absorption spectra (b) for ZMS and ZMS/AuNPs.

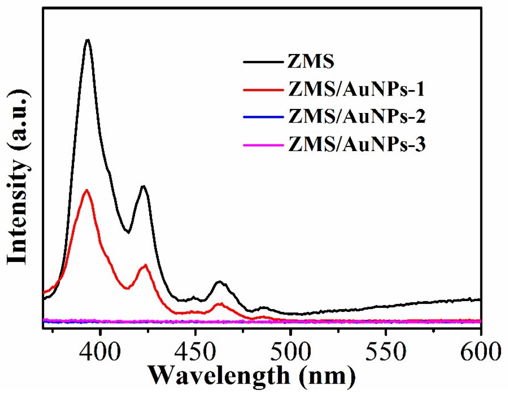

Fig. 8. PL spectra of the bare ZMS and ZMS-AuNPs heterstructures at various Au NPs concentrations.

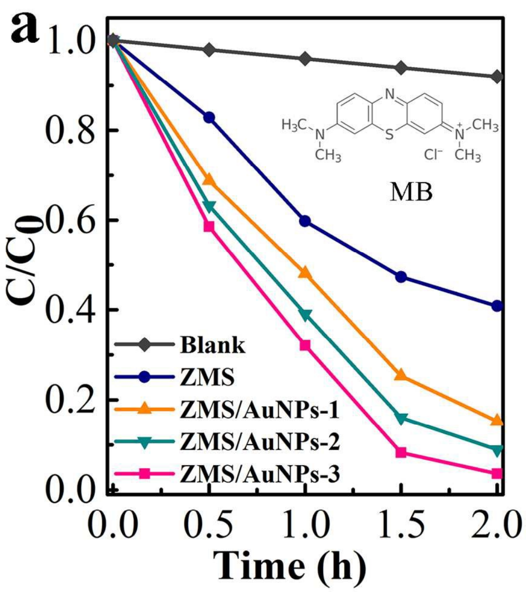

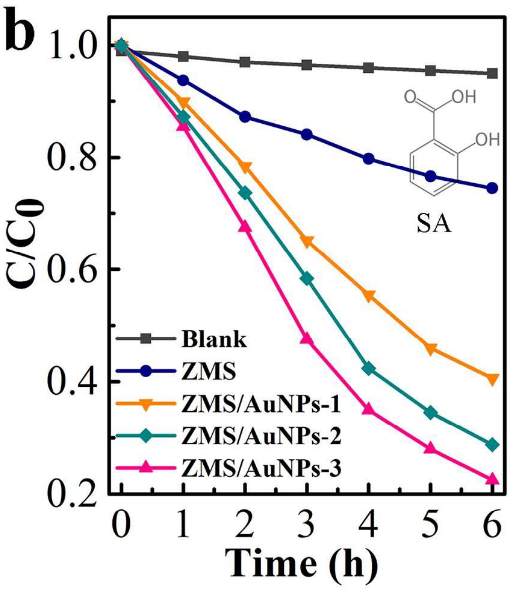

Fig. 9. Photocatalytic activity of ZMS and ZMS/AuNPs with different Au loading on the degradation of (a) MB and (b) SA under visible light, insets are the molecular structure of MB and SA, respectively.

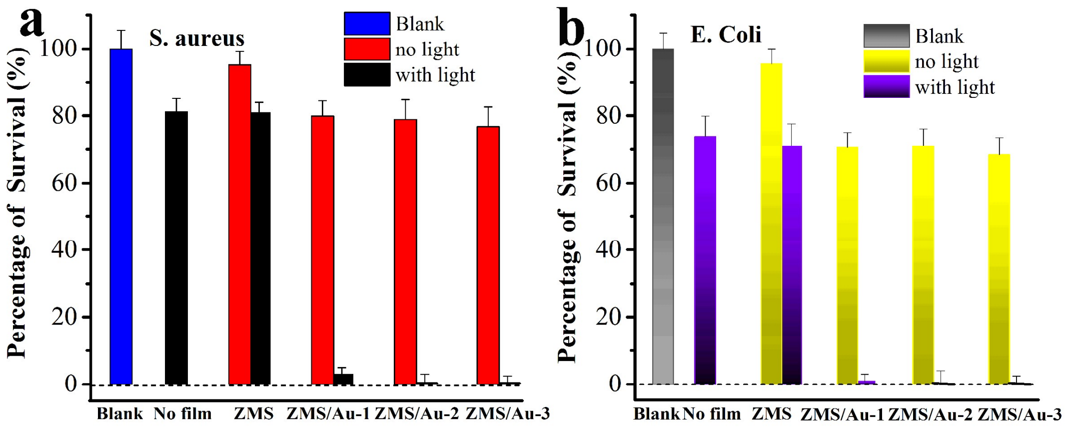

Fig. 10. Ability of ZMS and ZMS/AuNPs hybrid nanostructures in killing (a) S. aureus and (b) E. coli under visible light for 20 min. Blank represents bacteria exposed to neither NPs nor light. No film represents bacteria exposed to visible light but without catalyst. Grouped under ZMS, bacteria were exposed to ZMS alone or exposed to ZMS under visible light. Similarly, grouped under ZMS/Au-1, ZMS/Au-2 and ZMS/Au-3, bacteria were exposed to ZMS/Au-1, ZMS/Au-2 and ZMS/Au-3 alone, or exposed to visible light in the presence of ZMS/Au-1, ZMS/Au-2 and ZMS/Au-3.

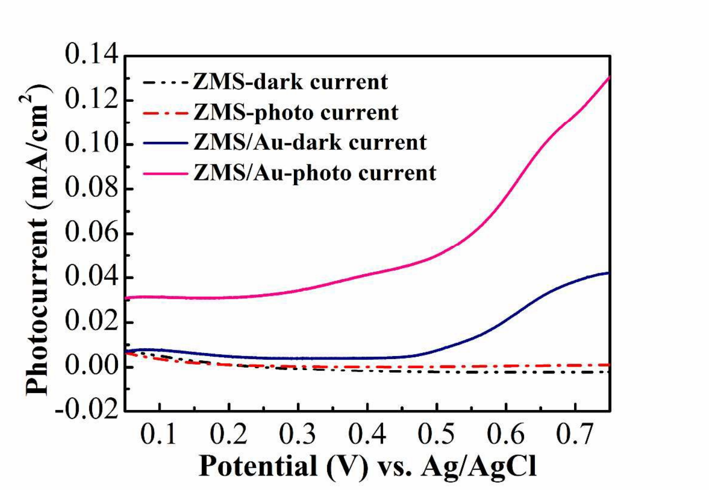

Fig. 11. I–V curves of ZMS and ZMS/Au under visible light illumination (>420 nm). Dashed curves: dark currents.

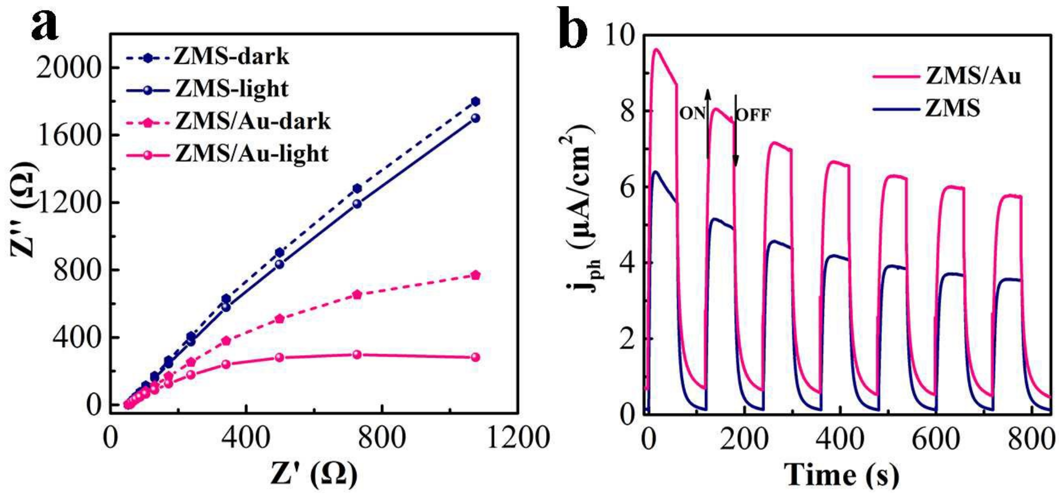

Fig. 12. (a) EIS Nyquist plots and (b) photoresponse of with light on/off cycles of ZMS and ZMS/Au under visible light illumination (>420 nm).